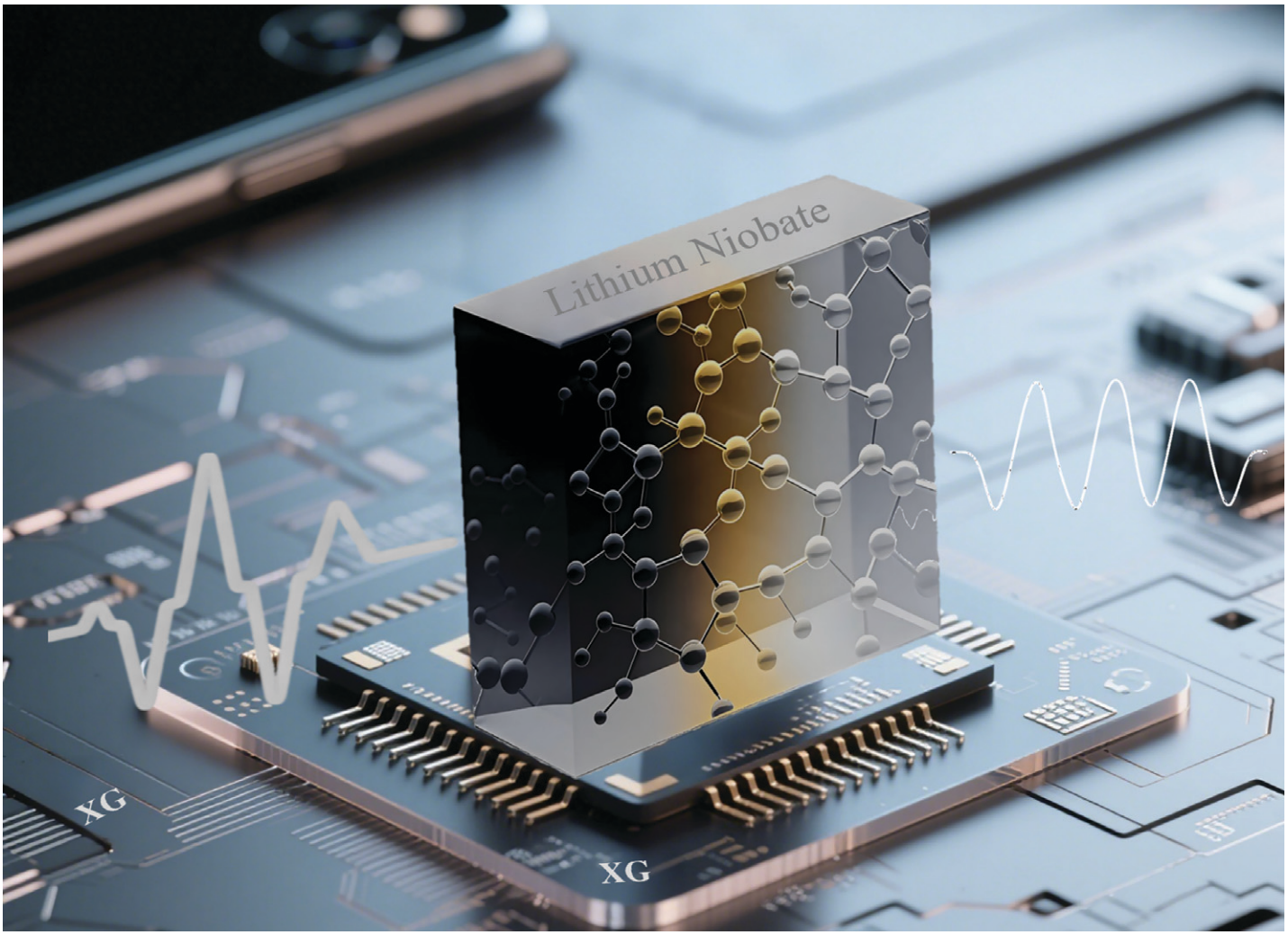

Showcasing research from Professor Kunfeng Chen's laboratory, Institute of Novel Semiconductors, Shandong University, Jinan, China.

Black lithium niobate single crystal: influence of point defects on its microwave properties

Lithium niobate piezoelectric crystal is widely used in various acoustic and microwave devices. Black lithium niobate crystals have different defect concentrations of bipolar, lithium vacancy, anti-site niobium etc. These defects can lead to lattice distortion and the formation of defect dipoles, which affect dielectric loss of acoustic devices.

Image reproduced by permission of Kunfeng Chen from *CrystEngComm*, 2025, **27**, 3238.

As featured in:

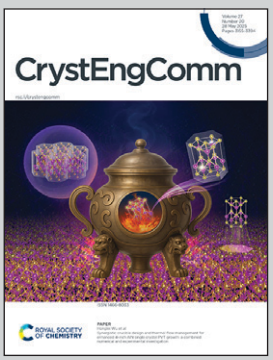

See Kunfeng Chen, Gongbin Tang, Dongfeng Xue *et al.*, *CrystEngComm*, 2025, **27**, 3238.

ROYAL SOCIETY OF CHEMISTRY

rsc.li/crystengcomm

Registered charity number: 207890

CrystEngComm

ROYAL SOCIETY OF CHEMISTRY

PAPER

View Article Online
View Journal | View Issue

Cite this: *CrystEngComm*, 2025, **27**, 3238

Black lithium niobate single crystal: influence of point defects on its microwave properties†

Yuneng Chen, [a] Zhongyang Liu,[a] Ming Li,[a] Zhiqiang Wang,[a] Zhenyu Li,[b] Kunfeng Chen, *[a] Gongbin Tang,*[a] Hui Hu[b] and Dongfeng Xue*[c]

Received 28th February 2025,
Accepted 11th April 2025

DOI: 10.1039/d5ce00220f

rsc.li/crystengcomm

Lithium niobate, as an important piezoelectric substrate material, is widely used in various acoustic and microwave devices. When lithium niobate crystals are grown from a melt at high temperatures, they typically contain a high concentration of intrinsic point defects. These point defects (either intrinsic or related to impurities or external fields) often alter the material's physical constants and increase acoustic losses. In this study, in order to study the effect of defects on the performance of SAW devices, we prepared black lithium niobate crystals with different concentrations of bipolarons, lithium vacancies, niobium anti-sites and other defects in an argon–hydrogen atmosphere. The types and concentrations of defects in the blackened lithium niobate wafers at different reduction temperatures were analyzed using UV-vis and IR spectroscopy. The chemical state of oxygen on the surface of the sample was analyzed by XPS. Dual-port electrodes were fabricated on the samples using micro-nano processing technology, and the relationship between the substrate dielectric loss and defects in lithium niobate was established through *S*-parameter testing. The results indicate that the chemical reduction treatment increases the defects in lithium niobate, leading to lattice distortion and the formation of defect dipoles, thereby increasing the dielectric loss of the devices. These findings provide profound insights into defect engineering for the application of lithium niobate in acoustic devices.

1 Introduction

Lithium niobate single crystals are multifunctional ferroelectric and piezoelectric crystals with a high Curie temperature (1210 °C), high electromechanical coupling coefficient, low dielectric loss, small temperature coefficient, piezoelectric effect, *etc.* As a result, it has found extensive application in optical, acoustic, and photoelectric devices.[1–5] The physical and chemical properties of lithium niobate primarily depend on its microstructure, defects, composition and size.[6–8] In recent years, with the rapid development of wireless communication technology, high frequency surface acoustic wave (SAW) devices play a crucial role in modern communication systems.[9,10] Compared with the commonly used piezoelectric crystal quartz, lithium niobate crystals and their films have a high sound velocity and can be used to prepare high-frequency SAW devices.[11,12] The stability of SAWs results from a combination of thermal stability and very low acoustic dissipation, as well as the temporal stability of the substrate's physical and chemical properties. The acoustic losses are highly dependent on the crystalline quality of lithium niobate used, which is characterized by point and extended defects, domains, impurities, *etc.*[13–15] Most of the point defects (intrinsic or related to impurities) of piezoelectric materials induce variations of the physical constants, of their temperature coefficients and, very often, a noticeable increase of the acoustic and/or of the dielectric dissipation.[16–18]

Although chemically reduced lithium niobate wafers (termed black lithium niobate) used for SAW devices have a high conductivity and opaque color, which minimizes pyroelectric effects and has a positive impact on the lithography process, the chemical reduction process also introduces many defects for lithium niobate. The existence of defects directly affects the operating frequency, bandwidth, substrate loss, temperature stability and other key performance indicators of high frequency SAW devices.[19,20]

Furthermore, various point defects of lithium niobate are inevitably introduced during the preparation and use of the device. These defects can affect the long-term frequency

[a] *Institute of Novel Semiconductors, State Key Laboratory of Crystal Materials, Shandong University, Jinan 250100, China. E-mail: kunfeng.chen@sdu.edu.cn, gongbin.tang@sdu.edu.cn*
[b] *School of Physics, Shandong University, Jinan 250100, China*
[c] *Shenzhen Institute for Advanced Study, University of Electronic Science and Technology of China, Shenzhen 518110, China. E-mail: dfxue@uestc.edu.cn*
† Electronic supplementary information (ESI) available. See DOI: https://doi.org/10.1039/d5ce00220f

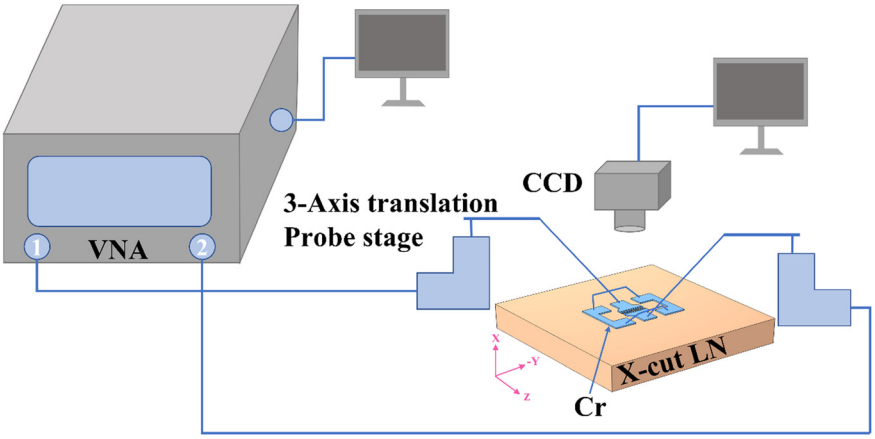

Fig. 1 Schematic diagram of *S*-parameter measurement of lithium niobate-on-wafer devices.

stability of microwave devices, *i.e.*, SAW, bulk acoustic wave (BAW), *etc.* Therefore, a deep understanding of the effect of defects on the physical and chemical properties of lithium niobate under various conditions is essential. In this study, we used ultraviolet and infrared spectroscopy to analyze the types and contents of defects in chemically reduced lithium niobate wafers at different temperatures. Two-port electrodes were prepared on black lithium niobate wafers combined with micro-nano processing technology. The *S*-parameters of the wafers in the frequency range of 0.1–1.7 GHz were tested, and the substrate loss values were calculated. Finally, the relationship between defects and lithium niobate substrate losses was analyzed, which lays a foundation for its application in acoustic and microwave devices.

2 Experimental section

2.1 Synthesis of black lithium niobate

X-cut lithium niobate wafers (10 mm × 10 mm × 0.5 mm, Guangzhou Zetian Electronics Co. Ltd.) were ultrasonically treated in acetone (AR, Tianjin Komiou Chemical Reagent Co. Ltd.), ethanol (AR, Tianjin Fuyu Fine Chemical Co. Ltd.) and deionized water successively to remove impurities on the surface of the wafers, and dried at 80 °C in an oven. Then the X-cut lithium niobate wafers were chemically reduced at 400 °C, 500 °C, 600 °C and 700 °C in a 95% Ar + 5% H_2 mixed atmosphere (heating rate: 10 °C min^{-1}, dwelling time: 2 h, cooled naturally).

2.2 Characterization of lithium niobate

Optical absorption was performed from 200 nm to 800 nm using a UV-vis spectrophotometer (UV-9000) with a spectral resolution of 0.5 nm. The samples were investigated by Fourier transform infrared spectroscopy (IR Affinity-1S) with a spectral resolution of 0.5 cm^{-1}. The O 1s spectra of the samples were analyzed using X-ray photoelectron spectroscopy (XPS, Thermo Scientific™ K-Alpha™$^+$), with C 1s (284.8 eV) as the reference, and a 100 W Al Kα ($h\nu$ = 1486.6 eV) X-ray source. The samples were analyzed under vacuum ($P < 10^{-8}$ mbar) with a pass

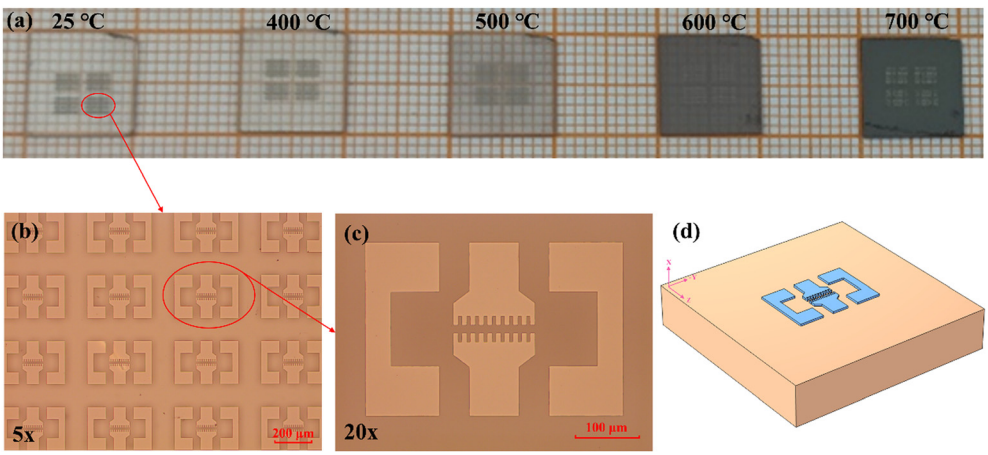

Fig. 2 (a) Morphology of X-cut lithium niobate wafers at different annealing temperatures. Micrographs of the electrode structure on the lithium niobate wafer at magnifications of (b) 5× and (c) 20×. (d) Schematic diagram of the electrode structure model on the lithium niobate wafer.

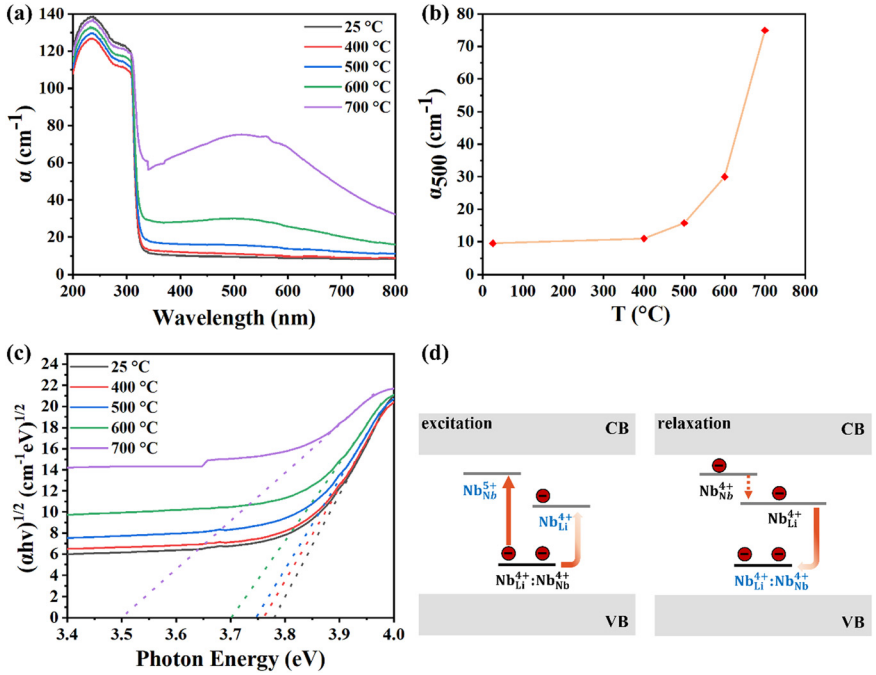

Fig. 3 (a) UV-vis absorption spectra of $LiNbO_3$ untreated (25 °C) and treated at different reduction temperatures (400 °C, 500 °C, 600 °C, and 700 °C). (b) The corresponding absorption coefficient values at λ = 500 nm for $LiNbO_3$ untreated (25 °C) and treated at different reduction temperatures (400 °C, 500 °C, 600 °C, and 700 °C). (c) The band gap values of $LiNbO_3$ untreated (25 °C) and treated at different reduction temperatures (400 °C, 500 °C, 600 °C, and 700 °C), which are obtained by the intercept method. (d) Generation and relaxation of small polarons in thermally reduced $LiNbO_3$.[28]

energy of 150 eV (survey scans) or 50 eV (high-resolution scans).

2.3 Two-port *S*-parameter measurement

Lithium niobate wafers untreated (25 °C) and treated at different chemical reduction temperatures (400 °C, 500 °C, 600 °C and 700 °C) were spin coated with a 1 μm thick photoresist (AZ1500). Laser direct writing lithography equipment (HEIDELBERG, MLA150) was used to engrave a two-port electrode pattern with a period of 14.1 μm (electrode tooth width of 6.3 μm) and an electrode spacing of 15 μm. Then, a layer of chromium film with a thickness of 120 nm was deposited on the wafer surface by magnetron sputtering. Acetone was used as the stripping solution to remove the photoresist to obtain the target electrode structure. Finally, a vector network analyzer (VNA, KEYSIGHT-E5071C, frequency range: 100 kHz–8.5 GHz) combined with a three-dimensional inspection station was used to measure the *S*-parameters and calculate its loss. The relationship diagram is shown in Fig. 1.

3 Results and discussion

To investigate the influence of point defects on the microwave properties of lithium niobate single crystals, we prepared blackened lithium niobate samples with varying defect concentrations by chemical reduction at different temperatures. As shown in Fig. 2a, compared to the untreated wafer (25 °C), the blackness of the treated wafers deepens with increasing reduction temperatures. Some studies suggest that the darkening of lithium niobate is primarily due to cation movement and the formation of small polarons/bipolarons. The coloration behavior is more likely related to bipolaron defects formed by niobium anti-sites.[21–24]

3.1 Ultraviolet-visible spectroscopy

UV-vis absorption spectrum measurements were conducted on lithium niobate treated at different chemical reduction temperatures (400 °C, 500 °C, 600 °C, and 700 °C), where the absorption coefficient α was calculated using the Lambert law:

$$I = I_0 e^{-\alpha d} \quad (1)$$

where I_0 is the initial light intensity, I is the light intensity after passing through the sample, and d is the sample thickness.[25]

Table 1 The band-gap value and the absorption coefficient at λ = 500 nm of lithium niobate untreated and under different reduction temperature treatments

Sample	Band gap	α_{500}
25 °C	3.78 eV	9.47 cm^{-1}
400 °C	3.76 eV	10.98 cm^{-1}
500 °C	3.75 eV	15.73 cm^{-1}
600 °C	3.70 eV	29.97 cm^{-1}
700 °C	3.50 eV	74.91 cm^{-1}

The characterization results are shown in Fig. 3a. Lithium niobate exhibits at least four different intrinsic small polarons, which generate characteristic absorption bands in the visible to near-infrared spectral range.[26] For the untreated sample, no significant absorption is observed in the entire visible region, and the absorption edge starts at approximately 320 nm. However, as the chemical reduction temperature increases (within the range of room temperature to 700 °C), the absorption edge of the treated samples gradually shifts toward longer wavelengths, showing a distinct red shift. This phenomenon is primarily attributed to changes in the defect states of Nb anti-sites (Nb_{Li}).[27] When the treatment temperature exceeds 500 °C, the absorption band significantly broadens with increasing reduction temperature, and a characteristic absorption peak appears at 500 nm (2.5 eV), corresponding to stable polaron pairs (Nb_{Li}^{4+}:Nb_{Nb}^{4+}), *i.e.*, small electron bipolarons.

Table 1 lists the absorption coefficients (α_{500}) at λ = 500 nm for the untreated sample and the samples treated at different temperatures. Fig. 3b further illustrates the trend of the bipolaron absorption band (α_{500}) intensity with increasing reduction temperature. It can be observed that the intensity of the bipolaron absorption band significantly increases with higher reduction temperatures, indicating that the bipolaron concentration rises as the reduction temperature increases.

In addition, the shift of the position of the absorption edge is also related to the transition energy of the valence electron from the 2p orbital of O^{2-} to the 4d orbital of Nb^{5+}. When the internal defects of lithium niobate crystals increase, the internal electron orbital transition energy will be reduced effectively.

We use Tauc's law and the transversal method to obtain the band gap values at different temperatures, and the results

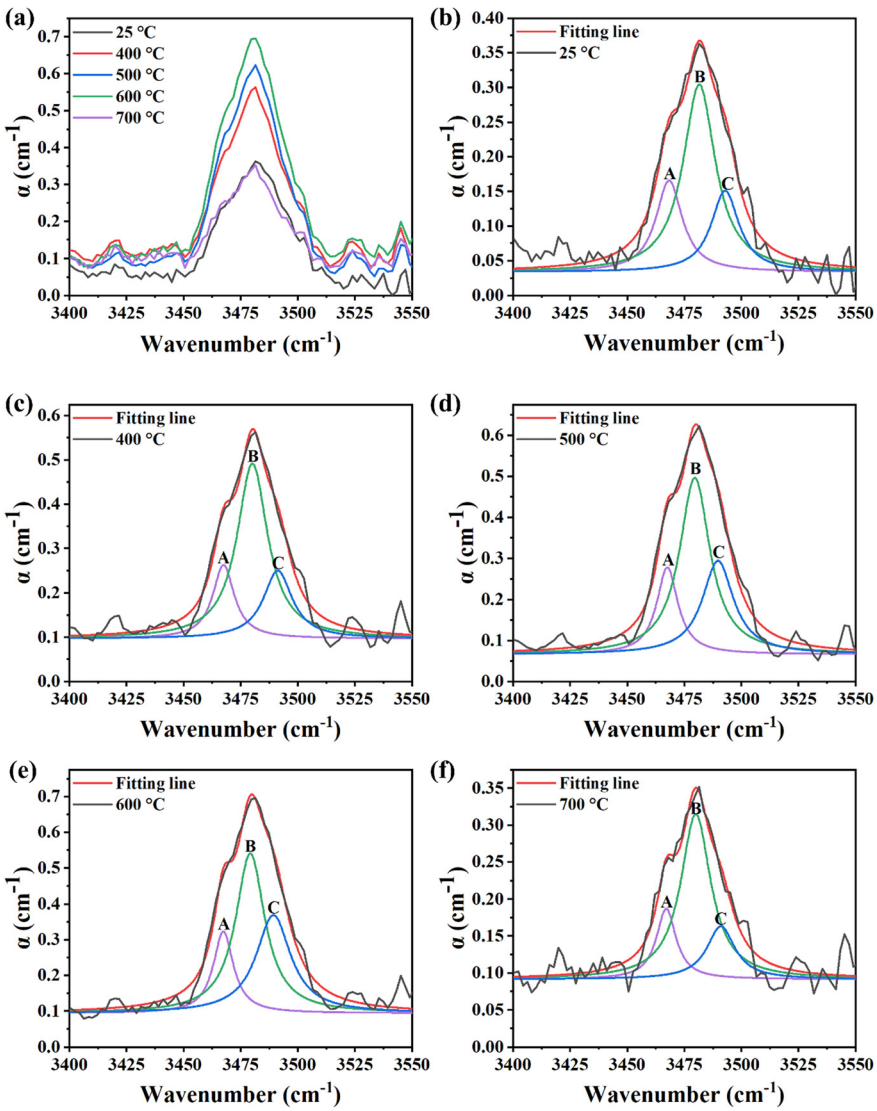

Fig. 4 (a) Infrared absorption spectra of $LiNbO_3$ untreated (25 °C) and treated at different reduction temperatures (400 °C, 500 °C, 600 °C, and 700 °C). Lorentzian multimodal fitting of the OH^- IR absorption spectra for $LiNbO_3$ wafers (b) untreated (25 °C) and reduced at temperatures of (c) 400 °C, (d) 500 °C, (e) 600 °C, and (f) 700 °C.

are recorded in Table 1.[29–31]

$$(\alpha h\nu)^{\frac{1}{2}} = K(h\nu - E_g) \quad (2)$$

As shown in Fig. 3c, the bandgap value of $LiNbO_3$ gradually decreases with increasing reduction treatment temperature. Consequently, the electrons on O^{2-} ions require less energy to transition from lower to higher energy states, resulting in the absorption of lower-energy photons. This shows that with the increase of reduction temperature, the internal defect concentration of lithium niobate increases, and the lattice disorder is enhanced, resulting in a redshift of the absorption edge.

3.2 Fourier transform infrared spectroscopy

Hydrogen is present in nearly all ABO_3 compounds; it forms an OH^- impurity complex and has an influence on the chemical and physical properties and applications.[32] $LiNbO_3$ crystals grown in air always contain protons and hydrogen atoms in the amount of 10^{16}–10^{18} cm^{-3}, bound to oxygen atoms of O_6 octahedra by hydrogen bonds. The presence of hydrogen atoms in the structure leads to the formation of complex defects of the type V_{Li}–OH and Nb_{Li}–OH.[33]

OH^- absorption spectra change with the varying Li composition of the crystal, because OH^- stretching vibration is sensitive to the environment around H^+. Thus, OH^- absorption spectra are frequently used as a probe for the crystal composition and lattice defects that affect the environment around H^+. Deformation vibrations of OH groups are supposed to manifest in the IR absorption spectra of LN crystals in the 3450–3550 cm^{-1} area.[34–36]

The OH^- absorption spectra of lithium niobate in the wavelength range of 3400–3550 cm^{-1} at different temperatures were characterized by Fourier transform infrared spectroscopy; the full spectrum is shown in Fig. S1.†

Fig. 4a shows the relationship between the absorption coefficient and the wavelength at different temperatures. As can be seen from the figure, with the gradual increase of the temperature, the absorption coefficient of the wafer also gradually increases, but at 700 °C, the absorption coefficient of the wafer drops and is similar to that at room temperature. The diminishing of OH-peak intensities may have been caused by the H-loss of the sample.

Through Lorentz multimodal fitting of the OH^- absorption spectra of lithium niobate wafers at different temperatures (shown in Fig. 4b–f, and detailed data are recorded in Table S1†), it is found that in all absorption bands, the positions of the decomposition peaks are at about 3466, 3481 and 3489 cm^{-1}, which are almost constant. These peaks are labeled here A, B, and C, respectively, in the order of wavelength from lowest to highest. This is due to some non-stoichiometric related defects (*e.g.*, Nb_{Li} and/or V_{Li}) that interfere with hydroxyl vibration.[37,38] Among them, the 3466 cm^{-1} infrared band is only sensitive to the defects of isolated V_{Li} capturing a proton; the 3481 cm^{-1} and 3489 cm^{-1} peaks are suggested to be associated with protons occupying intrinsic V_{Li} defects near Nb_{Li}^{5+}.[32,34,37]

In addition, we used the intensity ratio between ~3466 cm^{-1} (I_1) and ~3481 cm^{-1} (I_2) to calculate the Li_2O content in the wafer at different blackening temperatures.[36,39,40]

$$M = 50 - \frac{1}{1.933} \cdot \frac{I_1}{I_2} \text{ (mol \%)} \quad (3)$$

where M is the content of Li_2O in the sample in mol%. The results are shown in Table 2. As the temperature increases, the peak area at about 3466 cm^{-1} gradually decreases, and so does the Li_2O content. We calculate R using the M value [$R = M/(1 - M)$], and Li/Nb = R.

Knowing the Li/Nb value,[39,40] one can calculate the concentration of point defects [niobium anti-sites (Nb_{Li}^{4+}) and lithium vacancies (V_{Li})] in the LN crystal. Using a Li-vacancy compensation model, the concentration of Nb_{Li}^{4+} and V_{Li} point defects in mol% in a crystal lattice of nominally pure LN crystals can be calculated with the formula:[35,41,42]

$$C(V_{Li}) = \left(\frac{4 - 4 \times Li/Nb}{5 + Li/Nb}\right) \times 100 \text{ (mol \%)} \quad (4)$$

$$C(Nb_{Li}) = C(V_{Li})/4 \quad (5)$$

The calculation results are shown in Table 2. It can be observed that when the temperature exceeds 400 °C, the lithium content in the chemically reduced wafers decreases with increasing temperature, while the number of V_{Li} and Nb_{Li} defects increases. This is due to the lithium loss during the chemical reduction process, leading to the formation of lithium vacancies. This drives Nb^{5+} ions from Nb sites to occupy Li sites, simultaneously forming a large number of Nb_{Li}^{4+} defects. To maintain charge neutrality, each Nb_{Li}^{4+} requires four V_{Li} for charge compensation.

Table 2 Fitting peak strength, content of Li_2O in the sample in mol% (M), Li/Nb ratio, and concentration of Nb_{Li}^{4+} and V_{Li} defects of black lithium niobate

Sample	Crest number	Peak intensity (cm^{-1})	M (mol%)	R	$C(V_{Li})$	$C(Nb_{Li})$
25 °C	A	0.166	49.718	0.98878	0.74940	0.18735
	B	0.304				
	C	0.151				
400 °C	A	0.263	49.723	0.98898	0.73602	0.18401
	B	0.492				
	C	0.250				
500 °C	A	0.278	49.710	0.98847	0.77015	0.19254
	B	0.496				
	C	0.294				
600 °C	A	0.322	49.691	0.98772	0.82035	0.20509
	B	0.540				
	C	0.368				
700 °C	A	0.178	49.688	0.98760	0.82838	0.20710
	B	0.296				
	C	0.158				

Consequently, this inevitably leads to an increase in V_{Li} and Nb anti-site defects, which is consistent with the red shift of the absorption edge observed in lithium niobate after reduction treatment.[43,44]

3.3 X-ray photoelectron spectroscopy

X-ray photoelectron spectroscopy (XPS) is one of the most widely used surface analysis techniques. It can be applied to most solid materials, providing chemical state and valuable quantitative information from the material's surface. It can obtain information from a depth of approximately 10 nm from the surface. Defects in materials alter bonding energies, which can be observed through peak shifts or the emergence of new peaks. Therefore, compared to defect-free materials, XPS can serve as an effective method for detecting oxygen atoms or unsaturated sites in defective materials. Therefore, in order to explore the influence of different chemical reduction temperatures on the surface oxygen state of the sample, XPS technology was used to analyze the surface of the original sample and the samples treated with different temperatures. All peaks would be calibrated with the C 1s peak binding energy of 284.8 eV for adventitious carbon, and then the O 1s electron spectrum was fitted by the Gauss–Lorentz function mixture. The result is shown in Fig. 5. There are three fitting peaks in the O 1s electron spectrum.

Among them, the decomposition peak (O_1) near 530 eV corresponds to lattice oxygen, and the decomposition peak (O_3) near 530 eV corresponds to adsorbed oxygen. However, in most literature studies, the decomposition peak near 531 eV is attributed to oxygen vacancies.[45–48] Most of these studies only assume the presence of oxygen vacancies without sufficient evidence and do not consider the reversible phase separation/formation of Li_2O or the depletion of Li_2O on the surfaces. Due to this phase separation, without carefully monitoring the terminating surfaces, it is impossible to distinguish the oxygen movement in one direction from the

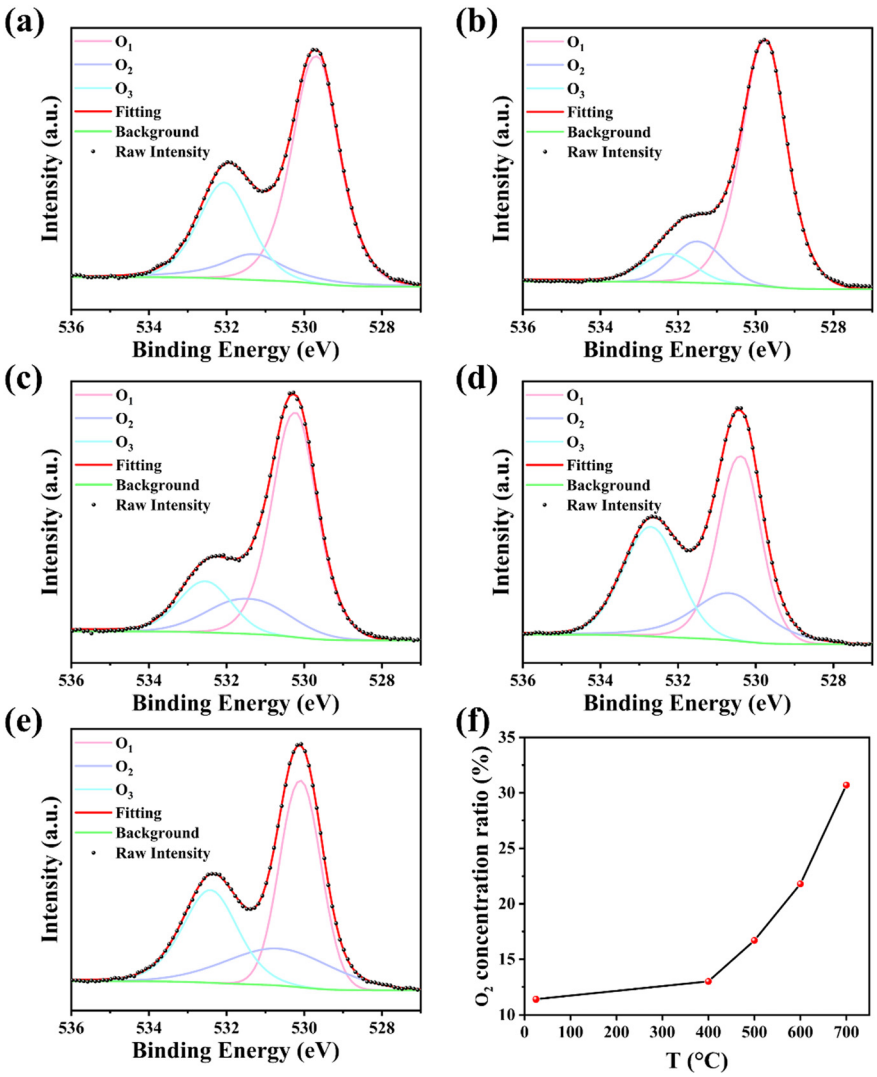

Fig. 5 (a) The O 1s electron spectra of $LiNbO_3$ wafers untreated at 25 °C and treated at different reduction temperatures: (b) 400 °C, (c) 500 °C, (d) 600 °C, and (e) 700 °C, fitted using a Gaussian–Lorentzian mixed function. (f) Plot of the O_2 concentration ratio on the surface of $LiNbO_3$ crystals untreated at 25 °C and treated at different reduction temperatures (400 °C, 500 °C, 600 °C, and 700 °C).

lithium movement in the opposite direction. A telling piece of evidence here is that in one experiment, the electrical conductivity values obtained using oxygen-specific electrodes on both sides of the sample, and those obtained using lithium-specific electrodes in another experiment, are of a similar order of magnitude.[49]

Moreover, the nature of the decomposition peak near 531 eV may be slightly different from that in other oxides. This might be because of oxygen atoms with different, weakly frustrated bonds on the internal surfaces or near-surface regions of Li_2O segregates. Alternatively, this could represent the depletion of oxygen near the surface of the sample. For this reason, in this paper, the decomposition peak near 531 eV is referred to as the surface state oxygen (O_2) of the sample. The concentration of the surface state oxygen of $LiNbO_3$ after treatment at different reduction temperatures was calculated based on the peak area ratio [$O_2/(O_1 + O_2 + O_3)$]. The measurement error of the peak area is 5%. As shown in Table S2,† with the increase in the treatment temperature, the concentration of the surface state oxygen of $LiNbO_3$ increases.

3.4 *S*-parameter measurement

A vector network analyzer is used to perform *S*-parameter two-port testing under small-signal power in the frequency range of 0.1 GHz to 1.7 GHz with a step size of 1 MHz. Fig. S2–S4† show the relationship between *S*-parameters, impedance, admittance, and frequency. Among them, impedance and admittance are reciprocal to each other. The microwave dielectric losses of the samples, both untreated (25 °C) and treated at different reduction temperatures (400 °C, 500 °C, 600 °C, and 700 °C), were calculated using the *S*-parameters.[50] The calculation error is ±0.01 dB.

$$L = 1 - |S_{11}|^2 - |S_{21}|^2 \quad (6)$$

As shown in Fig. 6a, at the same temperature, the microwave dielectric loss of the $LiNbO_3$ substrate increases with increasing frequency. To more intuitively observe the relationship between the substrate dielectric loss and different reduction temperatures, we selected five frequency points (0.1 GHz, 0.5 GHz, 1.0 GHz, 1.5 GHz, and 1.7 GHz) for comparative analysis. The results are shown in Fig. 6b. As the chemical reduction temperature increases, the substrate loss of the treated $LiNbO_3$ also increases. For example, at 0.1 GHz, compared to the untreated $LiNbO_3$ substrate, the substrate loss increases from 0.0022 dB to 0.0263 dB when the temperature reaches 700 °C. Table S3† provides more detailed data. Additionally, as clearly shown in Fig. S3,† which depicts the relationship between impedance and frequency, at certain frequencies (*e.g.*, 1 GHz or 1.5 GHz), the higher the chemical reduction temperature, the greater the impedance and, consequently, the greater the dielectric loss.

The microwave dielectric loss includes intrinsic and extrinsic losses, which are closely related to the type and concentration of defects. Intrinsic losses are primarily attributed to phonon scattering or defect-related anharmonic vibrations, while extrinsic losses are mainly influenced by secondary phases, oxygen vacancies, grain size, and densification or porosity. Based on our previous results, after chemical reduction treatment, the concentrations of defects such as bipolarons, V_{Li} and Nb_{Li} increase with higher reduction temperatures, and the electrical conductivity also increases. We speculate that the increase in dielectric loss may be due to the increased defects of $LiNbO_3$ after chemical reduction treatment, which cause lattice distortion. These defects form defect clusters or defect dipoles, hindering signal transmission and thereby increasing the dielectric loss of the device. The lattice distortion-induced disorder is primarily caused by two types of point defects: V_{Li} and Nb_{Li}^{4+}. These point defects may aggregate to form defect clusters, which further influence the dielectric loss.[13] At low frequencies and microwave bands, defect dipoles associated with substitutional ions also cause dielectric relaxation, leading to an increase in dielectric loss with higher substitution levels.[51–53]

4 Conclusions

In summary, we prepared blackened $LiNbO_3$ wafers at different reduction temperatures in an argon–hydrogen

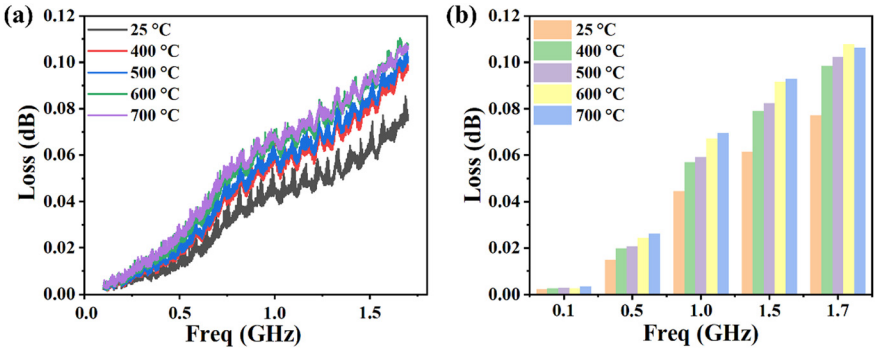

Fig. 6 (a) The relationship between the substrate loss of on-chip $LiNbO_3$ devices and frequency in the range of 0.1 to 1.7 GHz for untreated and treated samples at different reduction temperatures. (b) The substrate loss of on-chip $LiNbO_3$ devices at frequency points of 0.1 GHz, 0.5 GHz, 1.0 GHz, 1.5 GHz, and 1.7 GHz for untreated and treated samples at different reduction temperatures.

atmosphere and fabricated dual-port electrodes on them for microwave performance testing. The results show that as the chemical reduction temperature increases, more defects such as bipolarons, lithium vacancies, Nb anti-sites, and oxygen vacancies are generated in the samples. These defects reduce the internal electron transition energy, leading to an increase in lattice disorder, a red shift in the absorption edge, and a decrease in the bandgap. Furthermore, the presence of these defects affects the microwave dielectric loss of the $LiNbO_3$ substrate. As the chemical reduction temperature rises, the defect concentration in the treated samples increases, forming defect clusters or defect dipoles, which cause lattice distortion on the sample surface and result in higher dielectric loss. These findings provide valuable insights into the structural evolution and performance changes of defects in $LiNbO_3$-based microwave devices. In future work, we will continue to build on this foundation and further investigate the precise quantitative impact of each type of defect on device performance, aiming to meet the evolving demands of high-frequency acoustic devices.

Data availability

Data are available on request from the authors.

Conflicts of interest

There are no conflicts of interest to declare.

Acknowledgements

This work was supported by the National Natural Science Foundation of China (12204276, 52220105010) and the Natural Science Foundation of Shandong Province (ZR2021QF111, ZR202108100033). G. T. and K. C. also acknowledge the Qilu Young Scholars Program of Shandong University.

References

1 H. Feng, T. Ge, X. Guo, B. Wang, Y. Zhang, Z. Chen, S. Zhu, K. Zhang, W. Sun and C. Huang, *Nature*, 2024, **627**, 80–87.
2 T. Wu, L. Ledezma, C. Fredrick, P. Sekhar, R. Sekine, Q. Guo, R. M. Briggs, A. Marandi and S. A. Diddams, *Nat. Photonics*, 2024, **18**, 218–223.
3 M. Yu, R. Cheng, C. Reimer, L. He, K. Luke, E. Puma, L. Shao, A. Shams-Ansari, X. Ren, H. R. Grant, L. Johansson and M. Zhang, *Nat. Photonics*, 2023, **17**, 732.
4 Y. Chen, K. Chen and D. Xue, *Wujiyan Gongye*, 2024, **56**, 1–13.
5 A. Boes, L. Chang, C. Langrock, M. Yu, M. Zhang, Q. Lin, M. Fejer, J. Bowers and A. Mitchell, *Science*, 2023, **379**, 40.
6 K. Chen, J. Wu, Q. Hu, Z. Lu, X. Sun, Z. Wang, G. Tang, H. Hu and D. Xue, *Exploration*, 2022, **2**, 20220059.
7 K. Chen, Y. Zhu, Z. Liu and D. Xue, *Molecules*, 2021, **26**, 7044.
8 K. Chen, Y. Li, C. Peng, Z. Lu, X. Luo and D. Xue, *Inorg. Chem. Front.*, 2021, **8**, 4006–4013.
9 P. Liu, S. Fu, R. Su, H. Xu, B. Xiao, X. Zhou, S. Zhang, R. Wang, C. Song, F. Zeng, W. Wang and F. Pan, *IEEE Trans. Microwave Theory Tech.*, 2024, **72**, 5653–5666.
10 M. Li, X. Xia, K. Li, S. Wu, J. Zou, K. Chen and G. Tang, *IEEE Electron Device Lett.*, 2022, **43**, 1772–1775.
11 R. Takei, M. Suzuki, S. Kakio and Y. Yamamoto, *Jpn. J. Appl. Phys.*, 2024, **63**, 05SP16.
12 H. Xu, S. Fu, R. Su, P. Liu, B. Xiao, S. Zhang, R. Wang, C. Song, F. Zeng, W. Wang and F. Pan, *J. Microelectromech. Syst.*, 2024, **33**, 163–173.
13 G. Shi, K. Chen, G. Tang, H. Hu and D. Xue, *Guisuanyan Xuebao*, 2023, **51**, 1425–1438.
14 L. Kovacs, G. Corradi, Z. Szaller, L. Bencs, G. Mandula and K. Lengyel, *Phys. Rev. B*, 2024, **109**, 214105.
15 C. Kofahl, J. Uhlendorf, B. A. Muscutt, M. N. Pionteck, S. Sanna, H. Fritze, S. Ganschow and H. Schmidt, *Phys. Status Solidi A*, 2024, **221**, 2300959.
16 B. J. James, *Proceedings of the 42nd Annual Frequency Control Symposium 1988 (IEEE Cat. No. 88CH2588-2)*, 1988, pp. 146–154.
17 G. Tanvir, M. Saleem, H. Jabbar, A. Hamza, M. A. Hussain, M. Z. Khan, A. H. Baluch, M. Irfan, M. S. Butt, F. Naeem, A. Ghaffar, M. Ahsan, M. A. Rafiq, R. A. Malik and A. Maqbool, *Mater. Sci. Eng., B*, 2023, **287**, 116100.
18 J. Eom, G. Lee, M. Saleem, M. Ichimura, M. Z. Khan, M. B. Hanif, R. A. Malik and J. H. Koh, *J. Mater. Chem. C*, 2024, **12**, 19463–19475.
19 B. Capelle, J. Detaint and Y. Epelboin, *IEEE Trans. Ultrason. Ferroelectr. Freq. Control*, 2012, **59**, 1013–1022.
20 R. G. Gruenke, O. A. Hitchcock, E. A. Wollack, C. J. Sarabalis, M. Jankowski, T. P. Mckenna, N. R. Lee and A. H. Safavi-Naeini, *Sci. Rep.*, 2024, **14**, 6663.
21 O. F. Schirmer, M. Imlau, C. Merschjann and B. Schoke, *J. Phys.: Condens. Matter*, 2009, **21**, 123201.
22 O. F. Schirmer, O. Thiemann and M. Wohlecke, *J. Phys. Chem. Solids*, 1991, **52**, 185–200.
23 D. A. Dutt, F. J. Feigl and G. G. Deleo, *J. Phys. Chem. Solids*, 1990, **51**, 407–415.
24 G. Corradi and L. Kovacs, *Crystals*, 2021, **11**, 764.
25 I. Oshina and J. Spiguli, *J. Biomed. Opt.*, 2021, **26**, 100901.
26 C. Merschjann, B. Schoke and M. Imlau, *Phys. Rev. B: Condens. Matter Mater. Phys.*, 2007, **76**, 085114.
27 S. Saeed, H. Liu, L. Xue, D. Zheng, S. Liu, S. Chen, Y. Kong, R. Rupp and J. Xu, *Materials*, 2020, **13**, 5299.
28 J. Koppitz, O. F. Schirmer and A. I. Kuznetsov, *Europhys. Lett.*, 1987, **4**, 1055–1059.
29 K. Guithi, H. E. Sekrafi, A. B. Kharrat, K. Khirouni and W. Boujelben, *J. Opt.*, 2023, **52**, 1494–1506.
30 J. Tauc, *J. Mater. Res.*, 1968, **3**, 37–46.
31 Q. Luo, F. Bo, Y. Kong, G. Zhang and J. Xu, *Adv. Photonics*, 2023, **5**, 62–87.
32 Y. Kong, W. Zhang, X. Chen, J. Xu and G. Zhang, *J. Phys.: Condens. Matter*, 1999, **11**, 2139–2143.
33 N. A. Teplyakova, N. V. Sidorov and M. N. Palatnikov, *Opt. Spectrosc.*, 2020, **128**, 1131–1137.

34 K. Lengyel, A. Peter, L. Kovacs, G. Corradi, L. Palfalvi, J. Hebling, M. Unferdorben, G. Dravecz, I. Hajdara, Z. Szaller and K. Polgar, *Appl. Phys. Rev.*, 2015, **2**, 040601.
35 N. V. Sidorov, N. A. Teplyakova, O. V. Makarova, M. N. Palatnikov, R. A. Titov, D. V. Manukovskaya and I. V. Birukova, *Crystals*, 2021, **11**, 458.
36 A. Yatsenko, S. Yevdokimov, M. Palatnikov and N. Sidorov, *Ceramics*, 2023, **6**, 432–446.
37 L. Kovacs, L. Kocsor, Z. Szaller, I. Hajdara, G. Dravecz, K. Lengyel and G. Corradi, *Crystals*, 2017, **7**, 230.
38 H. Chen, L. Shi, W. Yan, G. Chen, J. Shen and Y. Li, *Chin. Phys. B*, 2009, **18**, 2372–2376.
39 G. Dravecz and L. Kovacs, *Appl. Phys. B: Lasers Opt.*, 2007, **88**, 305–307.
40 G. Dravecz, L. Kovacs, A. Peter, K. Polgar and P. Bourson, *Phys. Status Solidi C*, 2007, **4**, 1313–1316.
41 M. Y. Salloum, O. S. Grunsky, A. A. Man'shina, A. S. Tver'yanovich and Y. S. Tver'yanovich, *Russ. Chem. Bull.*, 2010, **58**, 2228–2232.
42 N. Iyi, K. Kitamura, F. Izumi, J. K. Yamamoto, T. Hayashi, H. Asano and S. Kimura, *J. Solid State Chem.*, 1992, **101**, 340–352.
43 X. Li, Y. Kong, H. Liu, L. Sun, J. Xu, S. Chen, L. Zhang, Z. Huang, S. Liu and G. Zhang, *Solid State Commun.*, 2007, **141**, 113–116.
44 T. Tian, X. Yan, Y. Kong, H. Liu, D. Zheng, S. Liu, S. Chen, J. Xu and J. Xu, *Crystals*, 2018, **7**, 368.
45 J. Song, C. Zhang, P. Zhao, B. Liu, C. Liu, P. Du, D. Mandler, W. Lei, Q. Guo and Q. Hao, *Chem. Eng. J.*, 2024, **485**, 150046.
46 J. Wang, X. Pan, W. Luo, Y. Shuai, H. Zeng, Q. Xie, S. Huang, C. Wu and W. Zhang, *Appl. Phys. Lett.*, 2022, **120**, 032901.
47 S. Fan, Q. Wang, Y. Hu, Q. Zhao, J. Li and G. Liu, *Chin. J. Chem. Eng.*, 2023, **62**, 132–138.
48 M. Sanad and A. Toghan, *Surf. Interfaces*, 2021, **27**, 101550.
49 S. Bredikhin, S. Scharner, M. Klingler, V. Kveder, B. Red'kin and W. Weppner, *J. Appl. Phys.*, 2000, **88**, 5687–5694.
50 H. C. Bell, *IEEE Microw. Mag.*, 2007, **8**, 70–76.
51 W. Guo, Z. Ma, Y. Chen, Y. Lu and Z. Yue, *J. Eur. Ceram. Soc.*, 2022, **42**, 4953–4961.
52 W. Guo, Y. Lu, Z. Ma, H. Wu and Z. Yue, *Acta Mater.*, 2023, **255**, 119093.
53 M. Qin, L. Zhang and H. Wu, *Adv. Sci.*, 2022, **9**, 2105553.

